Journal of Biomedical Optics

SPIEDigitalLibrary.org/jbo

Microscope-based near-infrared stereo-imaging system for quantifying the motion of the murine epicardial coronary arteries *in vivo*

David S. Long
Hui Zhu
Morton H. Friedman

SPIE

Microscope-based near-infrared stereo-imaging system for quantifying the motion of the murine epicardial coronary arteries *in vivo*

David S. Long,[a,b] Hui Zhu,[a] and Morton H. Friedman[a]
[a]Duke University, Department of Biomedical Engineering, Durham, North Carolina 27708
[b]University of Auckland, Auckland Bioengineering Institute, 70 Symonds Street, Auckland 1142, New Zealand

Abstract. Atherosclerosis is a leading cause of mortality in industrialized countries. In addition to "traditional" systemic risk factors for atherosclerosis, the geometry and motion of coronary arteries may contribute to individual susceptibility to the development and progression of disease in these vessels. To be able to test this, we have developed a high-speed (~40 frames per second) microscope-based stereo-imaging system to quantify the motion of epicardial coronary arteries of mice. Using near-infrared nontargeted quantum dots as an imaging contrast agent, we synchronously acquired paired images of a surgically exposed murine heart, from which the three-dimensional geometry of the coronary arteries was reconstructed. The reconstructed geometry was tracked frame by frame through the cardiac cycle to quantify the *in vivo* motion of the vessel, from which displacements, curvature, and torsion parameters were derived. Illustrative results for a C57BL/6J mouse are presented. [DOI: 10.1117/1.JBO.18.9.096013]

Keywords: atherosclerosis; coronary arteries; mice; arterial motion; stereo-imaging; near-infrared; three-dimensional image reconstruction; quantum dots.

Paper 130353R received May 16, 2013; revised manuscript received Aug. 2, 2013; accepted for publication Aug. 20, 2013; published online Sep. 20, 2013.

1 Introduction

Coronary artery atherosclerosis is a leading cause of morbidity and mortality in Western societies. Atherosclerosis is a progressive fibroinflammatory disease identified by intimal thickening, the focal accumulation of lipids, fibrous elements, and cellular elements within the walls of large arteries, known as atherosclerotic lesions.[1] Lesions preferentially develop at arterial branches, the outer walls of bifurcations, and the inner wall of curved sections; the cause of this focal vasculopathy is not fully understood. It is, however, understood from epidemiological and clinical studies that individual susceptibility to the development and localization of atherosclerotic lesions is influenced by systemic risk factors, including smoking, diabetes mellitus, obesity, hypertension, and high cholesterol. However, these risk factors cannot account for half of the variability in occurrence of this disease;[2,3] this indicates additional risk factors have not been identified. The epicardial coronary arteries, which are attached to the surface of the heart, undergo substantial motion during a cardiac cycle. Thus, one prevalent explanation of the focal nature of the disease is that the local fluid mechanical stresses at the walls of coronary arteries,[4] as well as mechanical stresses within the vessel wall, may mediate the phenotype of endothelial cells, thereby producing atherosusceptible sites.[5,6,7,8,9] Therefore, it has been speculated that certain aspects of arterial geometry and motion, which vary substantially among individuals, may increase an individual's susceptibility to developing atherosclerosis—geometric risk factors.[9,10,11]

To study the pathogenesis and evolution of disease, including atherosclerosis and the geometric risk factor, longitudinal studies are effective. However, in addition to limited patient availability and associated risks and costs, the slow progression and long asymptomatic phase of atherosclerosis in humans make longitudinal studies of early human atherosclerosis impractical. As a consequence, animals, in particular mice, have become important models for experimental atherosclerosis research.[12,13] Advantages of using the mouse are its short gestation period (~21 days), lower relative husbandry cost, and, in particular, the ability to knockout (or disrupt) endogenous genes associated with lipid metabolism and regulation.[14,15] The two most commonly used murine models of atherosclerosis are the low-density lipoprotein receptor deficient mouse ($LDLR^{-/-}$)[16] and the apolipoproteinE-deficient mouse ($apoE^{-/-}$). Even when fed normal chow, mice deficient in apoE develop hypercholesterolemia, with total plasma cholesterol levels nearly five times that of nonmutant mice, and spontaneously develop lesions that are phenotypically consistent, in composition and location, with those of human atherosclerosis.[17,18,19] Hence, we can advantageously use genetically modified mice to explore the geometric risk factor concept, if we can image the *in vivo* dynamics of the coronary arteries. Not withstanding these benefits and the availability of knockout models, cardiac imaging of mice is very challenging due to the small size of the heart (~8-mm major axis) and rapid heart rate (~500–600 beats/min). For those reasons, cardiac imaging of mice requires a comparable increase in both spatial and temporal resolution relative to that used in the clinical setting.

Address all correspondence to: David S. Long, University of Auckland, Auckland Bioengineering Institute, 70 Symonds Street, Auckland 1142, New Zealand. Tel: +64-9-923-1818; Fax: +64-9-367-7157; E-mail: d.long@auckland.ac.nz

Small-animal noninvasive imaging system resolution has increased with the use of respiratory and cardiac gating. Even so, current noninvasive imaging techniques such as micro-computed tomography (micro-CT),[20,21] magnetic resonance imaging (MRI),[22,23,24] and coronary microangiography[25] still lack sufficient resolution to dynamically image the motion of murine epicardial coronary arteries over a cardiac cycle. For example, to image cardiopulmonary structures in mice, Badea and colleagues[20] developed a micro-CT imaging system that uses cardiac and respiratory gating, and achieved an isotropic spatial resolution of 100 μm. However, since the diameter of the major murine coronary artery is on the order of 100 μm, this is insufficient spatial resolution and these images cannot be acquired real-time during a single heartbeat.[26] MRI has also been applied to small-animal imaging. For example, using cardiac-gated MRI to achieve a spatial resolution of 100 μm, Ref. 24 acquired images of the left coronary artery of a living mouse. However, these images were acquired only during mid-diastole, when cardiac motion is at a minimum. Reference 25 used *in vivo* microangiography to acquire digital images of murine coronary vessels less than ~500 μm in diameter at a pixel resolution of 7 μm. Although the spatial resolution of microangiography is significantly higher than that of gated micro-CT or MRI, it lacks sufficient temporal resolution since the maximum frame rate was 30 frames per second (fps). To acquire murine arterial motion data over a cardiac cycle, either an *ex vivo* heart preparation must be used, or the chest of the mouse must be opened to expose the beating heart; coronary arteries on a beating heart *in vivo* are more natural than those on an isolated heart.

Beyond the small heart size and rapid heart rate, optically imaging the murine coronary arteries has an additional challenge. As with other rodents, the murine coronary artery becomes intramyocardial just distal of its ostium,[27] so it is not easily distinguished from the myocardium, even under direct microscopic observation.[28] In order to image the dynamic motion of the artery, a fluorescence vascular contrast agent is then needed with four specific requirements: (1) minimal to no extravasation after introduction so that multiple successive cardiac cycles can be continuously imaged; (2) exceptionally bright and stable fluorescence signal so that paired images can be acquired at a sufficient frame rate (≥40 fps); (3) red-shifted (>650 nm) for increased tissue penetration to distinguish artery from myocardium; and (4) a small required intravenous injectate volume (<0.2 ml). We selected nontargeted near-infrared quantum dots (Qdots) that have an emission maximum wavelength of ~705 nm. Reference 29 reviewed the fabrication, properties, and use of Qdots for live-cell and *in vivo* imaging. Qdots are roughly protein-sized (~10 to 20 nm) bright fluorophores with a high quantum yield and are highly resistant to photobleaching. Qdots have been used in numerous *in vivo* imaging studies from whole animal,[30,31] to angiography of murine squamous cell carcinoma,[32] to microcirculation angiography,[33] and as intravascular probes.[34] Qdots are an ideal vascular contrast agent for imaging the *in vivo* dynamics of the murine coronary arteries.

To optically image the *in vivo* dynamics of murine epicardial coronary arterial segments over a single cardiac cycle, we have developed an imaging system. The system combines high-speed (~40 fps) near-infrared stereo-imaging into a standard microscope. The microscope is used as both the surgical microscope and the optics for the imaging system. Using this system, paired coronary artery images are synchronously acquired; the two images are calibrated and, under the constraints of epipolar geometry, the three-dimensional (3-D) vessel geometry is reconstructed. The reconstructed axis is tracked frame-by-frame to quantify the *in vivo* motion of the vessel. Illustrative results show that this system is a promising tool for laboratory investigations of vascular mechanics and experimental atherosclerosis.

2 Materials and Methods

2.1 *Animals and Surgery*

All animal experiments were conducted under a protocol approved by the Institutional Animal Care and Use Committee of Duke University and in accordance with the Guide for the Care and Use of Laboratory Animals (NIH Publication No. 85–23). Experiments were performed using a healthy male wild-type mouse (C57BL/6J, The Jackson Laboratory, Bar Harbor, ME), 15 weeks of age, weighing 29.2 g. The mouse was presedated with an intraperitoneal injection of ketamine (100 mg/kg, Fort Dodge Animal Health, Fort Dodge, IA) and xylazine (5 mg/kg, Lloyd Laboratories, Shenandoah, IA) and then placed in the supine position on an operating board and 38°C heating pad (Gaymar Industries Inc., Orchard Park, NY). The animal's body temperature was monitored throughout the entire procedure with a rectal temperature probe (RET-3, Physitemp Instruments, Clifton, NJ). An endotracheal tube was inserted perorally and a small-animal ventilator (~1.5 kPa ventilator pressure, ~100 breaths/min respiratory rate, SAR-830A/P, CWE Inc., Ardmore, PA) and an Isoflurane (1 to 2 vol.%) medical-oxygen mixture was used to maintain anesthesia during the procedure. A PE-10 polyethylene catheter (0.28 mm inside diameter, 0.61 mm outside diameter) was placed in the right external jugular vein for contrast agent infusion. To expose the left epicardial coronary artery for imaging, an oblique skin incision (~10 mm) was made just below (~2 to 3 mm) the animal's left axilla toward its xiphoid cartilage. The skin and pectoralis muscle were dissected away by blunt dissection so that the heart and left lung could be visualized through the intercostal muscles. A small incision (<10 mm) was made in the intercostal space between the fourth and fifth ribs counting from the xiphoid cartilage. Next, the ribs were gently retracted using a small-animal retraction system (Fine Science Tools, Foster City, CA). Using fine forceps, the pericardium was gently picked up and opened. The pericardium was attached to the animal's chest wall to provide a "natural cradle" for the heart. All mice were euthanized via exsanguination under anesthesia.

2.2 *Imaging System*

The imaging system shown in Fig. 1(a), which also served as the surgical microscope, consisted of a stereo-microscope (SMZ-1000) with a 0.5× objective (P-Plan Apo, numerical aperture of 0.012 at 0.8× zoom magnification and 0.05 at 8× zoom magnification), fluorescent filter attachment, and dual beam splitter (Nikon Instruments, Melville, NY), an excitation light source, a computer, a calibration pyramid, and two high-performance synchronized digital CCD cameras with 2 GB of internal memory (pco.1600, PCO-TECH, Romulus, MI). The angle of view difference between the two cameras was 6.3 deg. During image acquisition, the arterial images were stored on

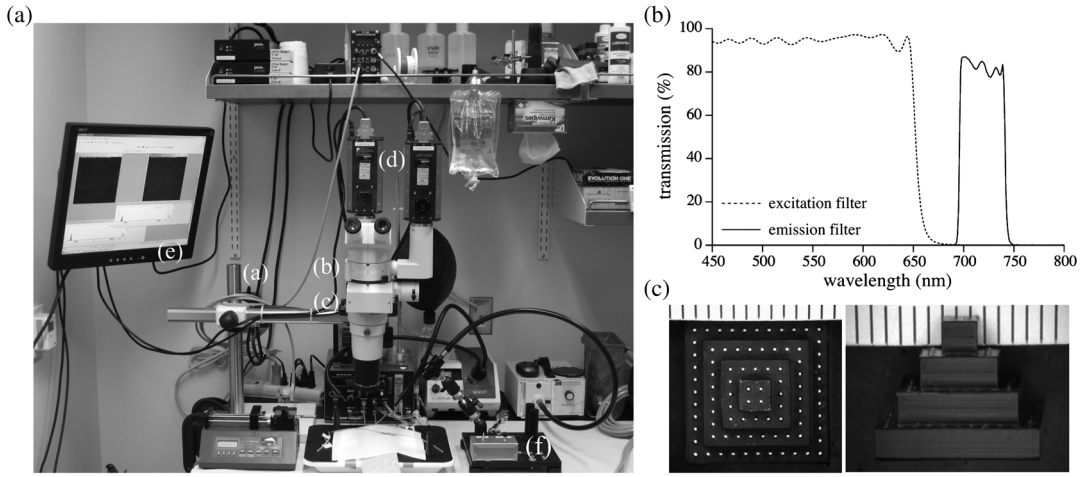

Fig. 1 (a) The microscope-based imaging system developed to quantify the motion of the murine epicardial coronary arteries consists of the following: (a) stereomicroscope, (b) dual beam splitter, (c) fluorescent filter attachment, (d) two high-performance synchronized CCD cameras, (e) computer monitor to observe the image acquisition, (f) an excitation light source, and a computer (not shown) to control the cameras. (B) The transmission spectra versus wavelength for the excitation filter (dashed line) and emission filter (solid line). (C) Photomicrographs of the top view (left image) and side view (right image) of the calibration pyramid used to calibrate the acquired images for image reconstruction. Note: The horizontal distance between marks corresponds to 1 mm.

the camera's internal memory and then, after each experiment, downloaded to a computer for image processing. The near-infrared emission light of the contrast agent was filtered using 18-mm diameter 690- to 730-nm bandpass emission filters (710AF40, Omega Optical, Brattleboro, VT). To excite the fluorescent contrast agent, a 150-W fiber-optic illuminator (Schott-Fostec, LLC, Auburn, NY) was used; it was outfitted with an EKE high-output halogen bulb (USHIO, Cypress, CA) and depleted of infrared wavelengths using a hot mirror (0 angle of incidence, Edmund Optics, Barrington, NJ). Attached to the illuminator was a liquid light guide (8 mm core diameter, 1 m long, Newport, Irvine, CA) and a fiber-optic focusing lens unit (Edmund Optics), which was modified to hold the 25-mm-diameter Qdot excitation filter (shortpass 650 nm cutoff, Edmund Optics) [see Fig. 1(b)]; the focusing unit was attached to an articulating arm mounting system to position the focusing unit during image acquisition. The calibration pyramid [see Fig. 1(c)] used in this study to define the imaging geometry was analogous to that used in previous biplane angiographic studies of human coronary arterial motion.[10,35] The pyramid was a black Delrin pyramid (11.5 mm × 11.5 mm base, 8.0 mm height) embedded with 88 0.5-mm-diameter stainless steel spheres (Salem Specialty Ball, Canton, CT), with the centroid of each sphere's relative location known.

2.3 *Imaging Contrast Agent*

In order to enhance the contrast between the left epicardial coronary artery and the epicardium for imaging, each mouse was intravenously administered nontargeted near-infrared Qdots (Qtracker 705, 2 μM, Invitrogen/Molecular Probes Inc., Eugene, OR, maximum emission wavelength of 705 nm) via the jugular vein catheter just before image acquisition. The Qdot solution was administered at a volume flow rate of 5 μl/s using a syringe pump (Kent Scientific Corporation, Torrington, CT) for a final injected concentration of ~8.5 pmol-Qdot/g animal weight, which for a 30-g mouse corresponds to a 100 μl injectate volume. Image was acquired immediately after injecting the contrast agent, and using the *pco.camware* software (PCO-TECH), a sequence of paired fluorescent arterial images (400 pixels × 400 pixels) was synchronously acquired at a frame rate of ~40 fps for two to three successive cardiac cycles, which corresponded to approximately eight frames per cardiac cycle. The paired images were acquired during a constant-pressure breath hold (pressure plateau). To achieve the breath-hold, the ventilator was switched to constant inhalation, and an external air pressure regulator (Type 70, 0 to 2 psi, Bellofram Corporation, Newell, WV) attached to the ventilator created a pressure plateau of ~15 cm H_2O, which was preset before experiments. After imaging the beating heart, the ventilator was reset to normal operation, and without disturbing the microscope, the animal was removed and replaced with the calibration pyramid in approximately the location of the animal's heart during image acquisition. Paired images of the calibration pyramid were acquired.

2.4 *Image Processing*

The image processing method used to reconstruct and track the 3-D murine coronary artery axis using a sequence of paired images was based on the technique developed for tracking human coronary arteries in biplane angiograms.[35,36] It involves three main steps: (1) calibrating the imaging system; (2) reconstructing the 3-D vessel axis in the first frame; and (3) tracking the 3-D vessel axis through the entire sequence of images.

2.5 *Imaging System Calibration*

At the time of image acquisition, the imaging geometry of the system was not known; therefore, a calibration process was needed to reconstruct a 3-D vessel axis from two two-dimensional (2-D) projection images of the vessel. The calibration process used in this study was described in greater detail elsewhere[35,36] and will only be summarized here. The 2-D position of each 0.5-mm-diameter stainless steel sphere in the calibration pyramid image was located by detecting circles using Hough

transform techniques. A projective transformation of a point from 3-D to a 2-D plane can be represented by

$$\begin{pmatrix} u \\ v \end{pmatrix} = \boldsymbol{T}(x, y, z) = \begin{pmatrix} \frac{c_{11}x+c_{12}y+c_{13}z+c_{14}}{c_{31}x+c_{32}y+c_{33}z+c_{34}} \\ \frac{c_{21}x+c_{22}y+c_{23}z+c_{24}}{c_{31}x+c_{32}y+c_{33}z+c_{34}} \end{pmatrix}, \quad (1)$$

where (u, v) is the 2-D coordinate of the point in the projection plane (image), and (x, y, z) is the coordinate of the point in the 3-D space. The coefficients $c_{11}, c_{12}, \ldots, c_{34}$ can be solved when six or more spheres are located in the image. For the stereo-imaging system, there were two projection transformations, $\boldsymbol{T}_1$ and $\boldsymbol{T}_2$, which represent, respectively, the first and second views obtained from each camera. Once the coefficients were determined, the projection transformations $\boldsymbol{T}_1$ and $\boldsymbol{T}_2$ were used to reconstruct the 3-D vessel axis.

2.6 *3-D Vessel Axis Reconstruction*

The axis of a coronary artery segment was modeled parametrically by a 3-D space curve, $p(s) = [x(s), y(s), z(s)]^T$, where x, y, and z were the 3-D coordinate functions, and $s \in [0, 1]$ were the parametric space along the length of the vessel axis. For a vessel point in one image, its corresponding vessel point in the other image could be located under the constraints of epipolar geometry, and the 3-D coordinates of this vessel point could be reconstructed. An initial plan for the vessel axis was obtained in the form of a bead chain by simply selecting several points along the axis and connecting them with straight lines. Assuming that the 3-D vessel axis projected into the intensity ridge in the two images, an energy function that was a combination of the intensities of the two images was minimized to refine the 3-D initial plan. The 3-D refined plan was then fit by a cubic spline curve and resampled at intervals of ~0.2 mm. This was the reconstructed axis of the 3-D vessel segment in the first frame of the image sequence.

2.7 *Vessel Tracking in 3-D*

After the 3-D vessel axis was located in the first pair of frames, it was automatically tracked for the remaining sequence of images. The frame-by-frame motion of the vessel was decomposed into two parts: (1) a global motion modeled by 3-D affine transformation and (2) a local motion of each point along the vessel axis, which makes the whole tracking model deformable. Similar to locating the initial plan in the first frame, the vessel was tracked by regarding its position in the previous frame as an initial guess. In addition to attracting the curve to the brightest position in the images, a string of small neighborhood windows along the vessel axis was set to be matched to the next frame, so that each point on the vessel could find its corresponding position at the next time point as accurately as possible.

2.8 *Quantification of Motion Parameters*

Once a vessel axis segment had been reconstructed and tracked from a sequence of paired images, it could be used to characterize coronary arterial motion, including torsion, τ, and curvature, κ. Curvature is a measure of how rapidly the curve changes direction at a point. Torsion is a measure of the rate at which the oscillating plane is turning along the vessel axis. These quantities could be determined using a cubic polynomial fitting method previously described.[36] For a given point, P, on the reconstructed 3-D vessel axis, a 2-mm window centered at P was selected. A half window typically contained five points. Within a window, the x, y, and z coordinates were individually fitted in a least squares sense to cubic polynomials:

$$\begin{aligned} x &= a_0 + a_1\eta + a_2\eta^2 + a_3\eta^3, \\ y &= b_0 + b_1\eta + b_2\eta^2 + b_3\eta^3, \\ z &= c_0 + c_1\eta + c_2\eta^2 + c_3\eta^3 \end{aligned} \quad (2)$$

where $\eta \in [-1, 1]$. Derivatives of x, y, and z with respect of η are taken and evaluated at $\eta = 0$ to determine torsion and curvature at P given by

$$\tau = \frac{[\boldsymbol{r}'(\eta) \times \boldsymbol{r}''(\eta)] \cdot \boldsymbol{r}'''(\eta)}{\|\boldsymbol{r}'(\eta) \times \boldsymbol{r}''(\eta)\|^2}, \quad (3)$$

$$\kappa = \frac{[\boldsymbol{r}'(\eta) \times \boldsymbol{r}''(\eta)]}{\|\boldsymbol{r}'(\eta))\|^3}, \quad (4)$$

where $\boldsymbol{r}(\eta) = x(\eta)\hat{\boldsymbol{e}}_x + y(\eta)\hat{\boldsymbol{e}}_y + z(\eta)\hat{\boldsymbol{e}}_z$.

2.9 *Validation with a Coronary Arterial Phantom*

To assess the capabilities of this stereo-imaging system and the 3-D reconstruction process, we constructed, imaged, and then reconstructed the geometry of a coronary artery phantom whose shape was known. The phantom was constructed to closely represent both the size and 3-D path of the main murine coronary artery.[37] The phantom artery was a 5.25-mm space curve engraved into an ~8-mm-diameter acrylic cylinder [see Fig. 2(a)]. The path of the phantom was described parametrically by the following equations:

$$x = R\ \sin\ \theta, \quad y = -\frac{h}{2}\ \sin 4\theta, \quad \text{and} \quad z = R(1 - \cos\ \theta), \quad (5)$$

where R is the radius of the cylinder, $h = 4$ mm, and the parameter θ ranges from $-\pi/8$ to $\pi/8$. [Note: the x-y-z coordinate system is defined in Fig. 2(a).] The phantom artery was placed under the imaging system, and under epi-illumination, paired images of the phantom were acquired. Without disturbing the microscope, the phantom was replaced with the calibration pyramid and paired images of it were acquired. Using these images, the imaging system was calibrated and the 3-D phantom axis was reconstructed.

3 Results

3.1 *Results of Coronary Arterial Phantom Validation*

Paired images were acquired of the 5.25-mm-long phantom coronary artery [Fig. 2 (a), black curve]. The phantom coronary artery axis was reconstructed. Superimposed on each image in Fig. 2(a) is the reconstructed 3-D axis of the phantom [Fig. 2(a), dotted white curve] and, on the left image, the coordinate system. The actual phantom axis, defined by the parametric equations in Eq. (5), was compared against the reconstructed 3-D phantom axis and shown in Fig. 2, (b) the x-y plane, (c) the z-y plane, and (d) the z-x plane. The root-mean-square (RMS) error for the x, y, z coordinate was 0.010, 0.011, and

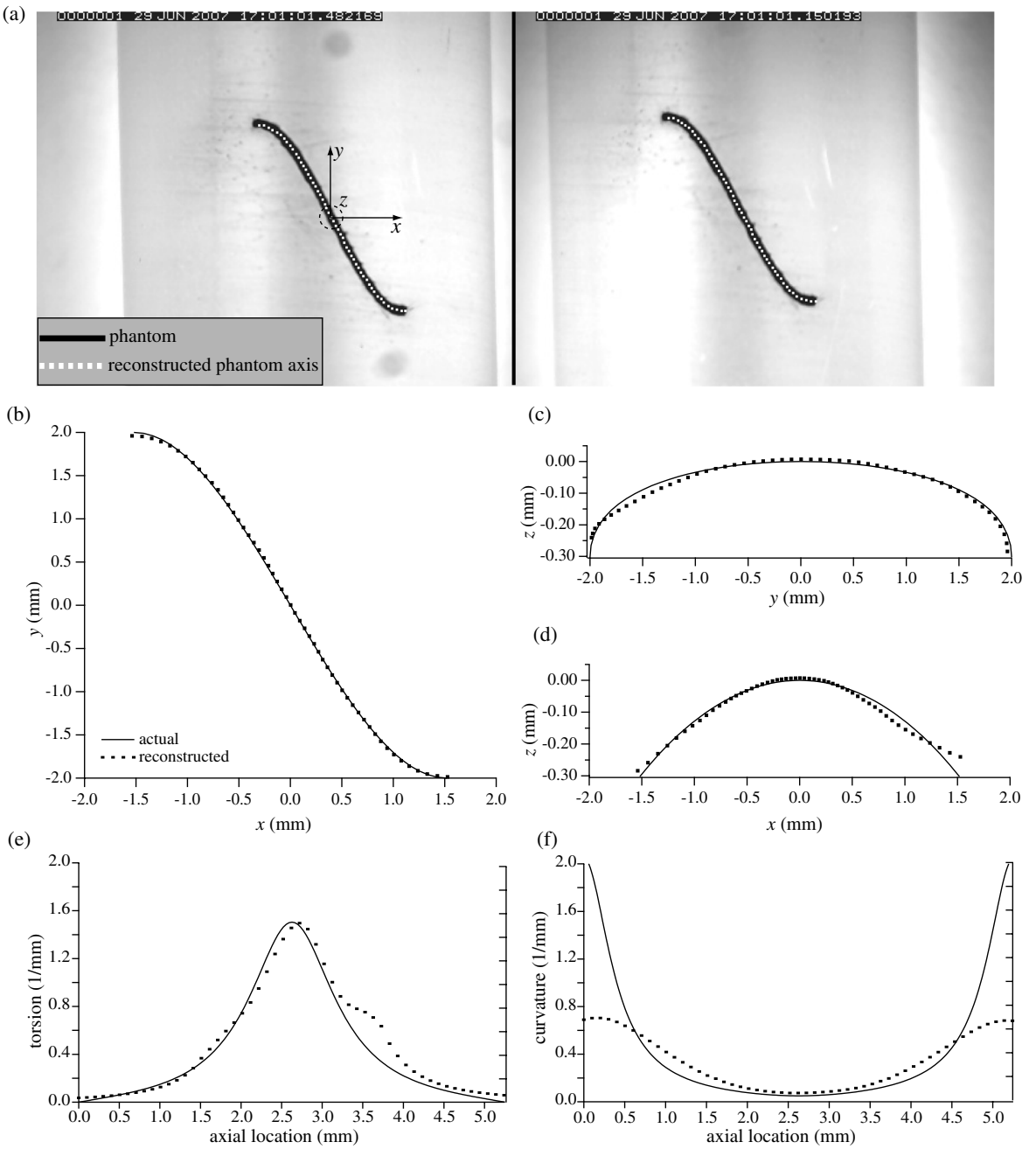

Fig. 2 (a) Paired images of the 5.25-mm-long phantom coronary artery (black curve) with the reconstructed three-dimensional (3-D) axis of the phantom (dotted white curve) superimposed on each image and, on the left image, the coordinate system. The phantom geometry is described parametrically by $x = R \sin\theta$, $y = -0.5\ h \sin(4\theta)$, and $z = R(1 - \cos\theta)$, where R is the radius of the cylinder ($R = 4$ mm), $h = 4$ mm, and θ ranges between -22.5 and 22.5 deg. Comparison between the phantom axis given by the parametric equation and the reconstructed 3-D phantom axis in (b) the x-y plane, (c) the z-y plane, and (d) the z-x plane. Comparison between the actual values (solid curves) of the phantom axis and the values calculated from the reconstructed phantom axis (dotted curves) of (e) torsion and (f) curvature along the phantom axis.

0.014 mm, respectively. In this figure, the solid line represents the value of interest for the actual phantom axis and the dotted line represents the value of interest for the reconstructed phantom axis. Point-by-point comparison was made between the actual values (solid curves) of the phantom axis and the values calculated from the reconstructed phantom axis (dotted curves) of (e) torsion and (f) curvature along the phantom axis. The RMS error in torsion was 0.098 mm^{-1}, whereas the RMS error in curvature was 0.74 mm^{-1}.

3.2 *Results of In Vivo Coronary Artery Motion*

3.2.1 *3-D vessel axis reconstruction*

The imaging system was used to quantify the motion of a left epicardial coronary artery segment of a 29.2-g male C57BL/6J mouse. The mouse was intravenously injected with ~8.5 pmol/g of nontargeted, near-infrared Qdots and then imaged at a frame rate of 40 fps. Illustrative paired fluorescence images are shown in Fig. 3(a) for one instant in a cardiac cycle.

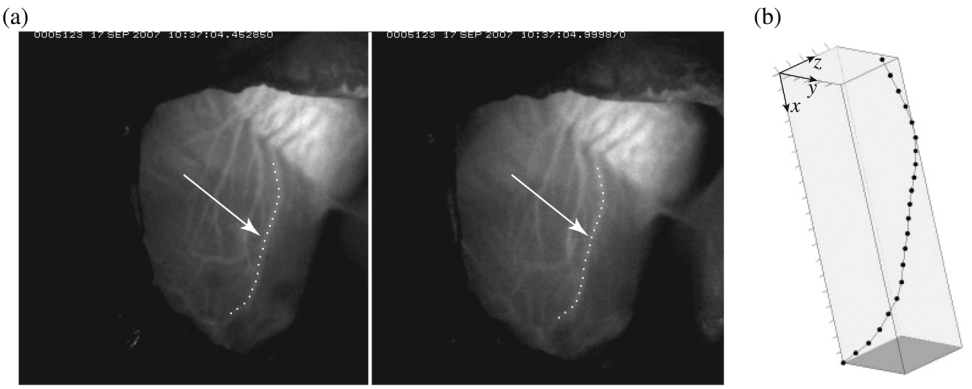

Fig. 3 (a) Paired fluorescence images of the main branch of the left epicardial coronary artery *in vivo* (denoted by arrow) on the beating heart of a 29.2-g C57BL/6J mouse imaged, at a frame rate of ~40 fps, with the stereo-imaging system shown in Fig. 1. The mouse was intravenously injected with ~8.5 pmol/g of nontargeted, near-infrared quantum dots imaging contrast agent. Superimposed on each image in (a) is the 3-D reconstructed vessel axis segment (dotted white line). (b) For the paired images in (a), the 4.3-mm-long reconstructed segment of the vessel axis is calculated from 22 locations spaced 0.2 mm along the vessel axis and displayed in approximately the same orientation of the heart in (a). Note: The distance between axis tick marks is 0.2 mm.

For that instant, a 4.3-mm-long left coronary artery segment was reconstructed [Fig. 3(b)]. Using the reconstructed vessel axis, the torsion and curvature of the vessel centerline was determined. For this instant in the cardiac cycle, the vessel centerline torsion ranged from a minimum of 0.02 mm^{-1} to a maximum of 4.62 mm^{-1} with a mean torsion of 0.95 mm^{-1}, whereas the vessel centerline curvature ranged from a minimum of 0.13 mm^{-1} to a maximum of 1.22 mm^{-1} with a mean curvature of 0.48 mm^{-1}. Once the vessel axis was reconstructed for one instant in a cardiac cycle, the motion of the vessel axis was tracked and the frame-by-frame motion determined.

3.2.2 *Vessel tracking in 3-D*

Over two successive cardiac cycles, paired fluorescence images of the left coronary of a C57BL/6J mouse were acquired at ~40 fps (eight frames per cardiac cycle). Figures 4(a) to 4(c) show paired fluorescence images at (a) frame 1, (b) frame 4,

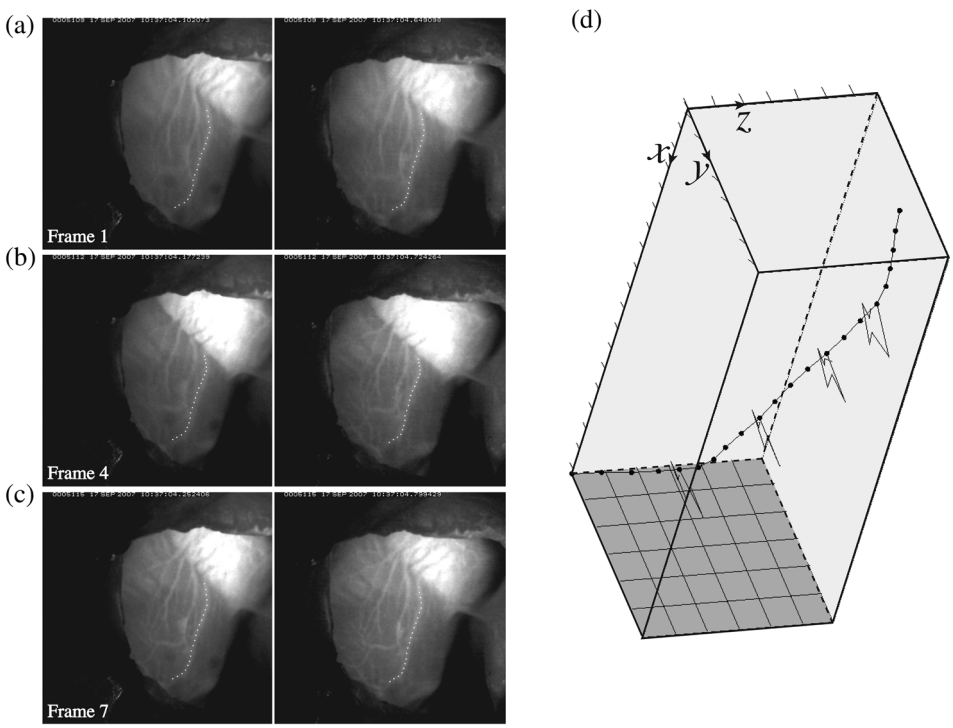

Fig. 4 (a) to (c) Paired fluorescence image sequence of the left coronary artery of a C57BL/6J mouse acquired at a frame rate of 40 fps with the stereo-imaging system shown in Fig. 1. Superimposed on each image in (a) to (c) is the reconstructed vessel axis (dotted line) for that pair of images. The images are from the (a) first, (b) fourth, and (c) seventh frames during a cardiac cycle for which a total of eight frames were acquired. (d) A reconstructed axis (solid line) of the left coronary artery from the initial plan (i.e., first frame of cardiac cycle) (a), with trajectories, covering the first seven frames during a cardiac cycle [shown in (a) to (c), attached at four selected axial locations. Note: On each axis in (d), the distance between axis tick marks is 0.2 mm.

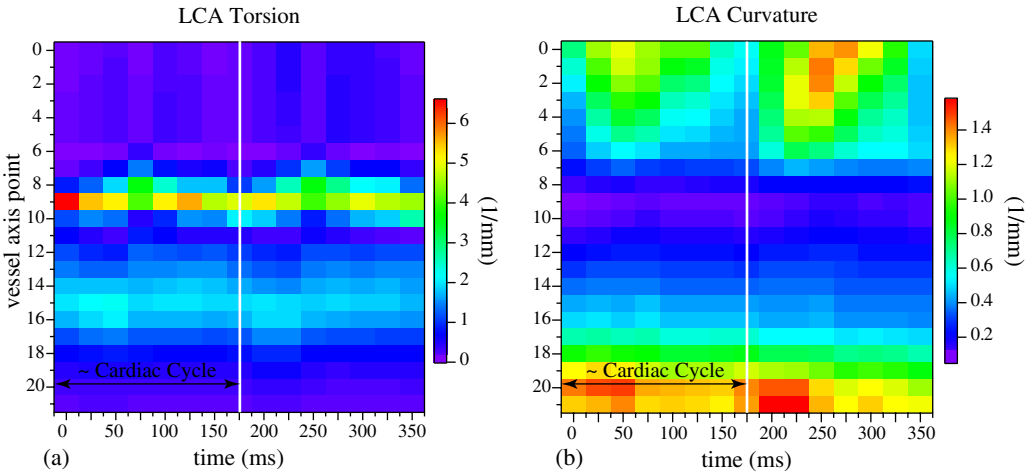

Fig. 5 For two sequential cardiac cycles, a pseudocolor plot of the variation with axial position and time of (a) torsion and (b) curvature of the left epicardial coronary artery segment shown in Fig. 4.

and (c) frame 7 of a cardiac cycle. As illustrative results, trajectories at four axial locations are shown in Fig. 4(d). Over the two successive cardiac cycles, the total vessel axis arc length ranged from a minimum of ∼3.6 mm to a maximum of ∼4.3 mm.

3.2.3 *Quantification of motion parameters*

Using the tracked and reconstructed sequence of images shown in Fig. 4, the temporal and spatial variations of motion parameters were determined. Figure 5 is a pseudocolor plot that shows the temporal and spatial variation of (a) torsion and (b) curvature for two successive cardiac cycles, with the first cardiac cycle corresponding to results shown in Fig. 4.

The variations in torsion and curvature were calculated from a reconstructed image sequence of 15 frames that was captured at 40 fps. Vessel axis point 0 corresponds to the proximal end of the reconstructed segment, whereas point 21 corresponds to the distal end of the reconstructed vessel segment. These quantities, as seen in Fig. 5, vary both spatially and temporally during each cardiac cycle. Over the two successive cardiac cycles, the vessel axis torsion ranged from a minimum of 0 mm^{-1} to a maximum of 6.59 mm^{-1} with a mean torsion of 1.11 mm^{-1}. The vessel axis curvature ranged from a minimum of 0.05 mm^{-1} to a maximum of 1.58 mm^{-1} with a mean curvature of 0.57 mm^{-1}.

4 Discussion

In summary, we presented a microscope-based stereo-imaging system and image reconstruction and motion tracking process that is capable of quantifying the *in vivo* dynamics of the murine coronary arteries. Illustrative imaging and reconstruction results for C57BL/6J mouse were presented. The reconstructed vessel axis geometry was tracked frame by frame through two successive cardiac cycles to quantify the *in vivo* motion of the vessel segment, and displacements, curvature, and torsion parameters were determined. We have restricted the imaging to the left coronary artery. As reviewed by Ref. 38, it appears that human coronary artery atherosclerosis is more prevalent in the left coronary artery than the right coronary artery. Although the hemodynamics and anatomical differences between these two arteries may play a role, the pathophysiological mechanisms involved remain unknown.

This microscope-based stereo-imaging system complements small-animal noninvasive cardiac imaging systems such as MRI and micro-CT. Key features/benefits of the present system include (1) the use of near-infrared Qdots, which provide increased tissue penetration and are resistant to photobleaching and extravasation, allowing successive cardiac cycle imaging; (2) sufficient temporal resolution to permit measurement of murine epicardial coronary arterial dynamics during a cardiac cycle; (3) the use of stereoscopy for 3-D imaging; and (4) the ability to support serial studies.

All Qdots when continuously excited exhibit fluorescence intermittency (blinking) and, therefore, spontaneously alternate between emitting (on) and nonemitting (off) states. This alternating is most easily observed in single Qdot tracking/imaging;[39,40] it can also be exploited to verify the presence of single Qdots due to their blinking, or clusters of Qdots due to their apparent nonblinking.[41] Moreover, fluorescence intermittency does not substantially impact measurements/imaging of ensemble or clusters of Qdots, such as the case for vascular contrast agents. Previous studies have reported the use of Qdots as a vascular contrast agent with blinking not adversely affecting their measurements.[30,42]

Because optical imaging is used, the animal's chest must be surgically opened to expose the beating heart. In a study of the differences in hemodynamics and force–frequency relationships between the open-chest and closed-chest mouse models, Ref. 43 determined that differences in these factors do, in fact, exist. In these earlier experiments, a bilateral thoracotomy was employed. The surgical technique used in the present work is based on the survival surgical procedure used in coronary artery ligation studies, which is much less invasive than a thoracotomy and may result in a smaller alteration of thoracic mechanics. Because a survival surgical procedure is used, the experimental system described here can be used in serial studies if tissue collection is not needed at intermediate time points.

One of the central goals of atherosclerosis research is to identify risk factors of the disease to promptly identify individuals at risk, or to improve the prognosis of diagnosed individuals. We believe that specific coronary arterial kinematics will be directly correlated to the initiation and progression of atherosclerotic lesions in these vessels. For example, in recent studies of the dynamics of human coronary arteries,[36,35] it was found that

the motion of the left anterior descending artery is much different than that of the right coronary artery: (1) less displacement and (2) greater axial variation in torsion. The motion parameters were also found to vary greatly between individuals and along an individual vessel axis. Motion parameters that exhibit large axial variations might be related to variations in susceptibility to atherosclerosis. No studies have integrated the analysis of motion parameters, histomorphometry, and genomics. We have developed a microscope-based stereo-imaging system capable of imaging the *in vivo* motion of murine epicardial coronary arteries. Using the system described in this paper, we can investigate whether certain arterial motions produce a pro-atherogenic environment, by imaging the coronary arteries of apoE-deficient mice with different stages of disease, followed by histological and genomic characterization. In future studies, this stereo-imaging system could be used to investigate the relationship between the motion of epicardial coronary arteries and the degree of atherosclerotic change in those vessels. Researchers have established[18] that mice deficient in apoE and on normal chow spontaneously develop most of the pathological aspects (i.e., composition and sites of disease) of human atherosclerosis over a few months. This relatively short time-to-disease, compared to that of humans, and the imaging system described herein will enable a serial study of atherosclerosis that integrates arterial motion parameters, histomorphometry, and genomics using a mouse model that is relevant to the disease in humans.

Acknowledgments

This work was supported by National Institutes of Health grants HL058856 (M. H. F., H. Z.) and HL083715 (D. S. L.). The authors would like to thank Dr. Lan Mao (Department of Medicine, Duke University) for training in mouse cardiac surgery and Ellen Dixon-Tulloch (Department of Biomedical Engineering, Duke University) for assistance with animal studies.

References

1. R. Ross, "Atherosclerosis—an inflammatory disease," *N. Engl. J. Med.* **340**(2), 115–126 (1999).
2. T. Pearson, "Coronary arteriography in the study of the epidemiology of coronary disease," *Epidemiol. Revs.* **6**(1) 1984).
3. J. R. Crouse, "Progress in coronary artery disease risk-factor research: what remains to be done?," *Clin. Chem.* **30**(7), 1125–1127 (1984).
4. W. C. Aird, "Endothelial cell heterogeneity and atherosclerosis," *Curr. Atheroscler. Rep.* **8**(1), 69–75 (2006).
5. C. G. Caro, J. M. Fitz-Gerald, and R. C. Schroter, "Atheroma and arterial wall shear, observation, correlation and proposal of a shear dependent mass transfer mechanism for atherogenesis," *Proc. R. Soc. Lond. B Biol. Sci.* **177**(1046), 109–159 (1971).
6. W. C. Aird, "Phenotypic heterogeneity of the endothelium: II. Representative vascular beds," *Circ. Res.* **100**(2), 174–190 (2007).
7. S. G. Frangos, V. Gahtan, and B. Sumpio, "Localization of atherosclerosis—role of hemodynamics," *Arch. Surg.* **134**(10), 1142–1149 (1999).
8. A. G. Passerini et al., "Coexisting proinflammatory and antioxidative endothelial transcription profiles in a disturbed flow region of the adult porcine aorta," *Proc. Natl. Acad. Sci. U S A* **101**(8), 2482–2487 (2004).
9. M. H. Friedman et al., "Relationship between the geometry and quantitative morphology of the left anterior descending coronary artery," *Atherosclerosis* **125**(2), 183–192 (1996).
10. Z. H. Ding and M. H. Friedman, "Dynamics of human coronary arterial motion and its potential role in coronary atherogenesis," *J. Biomech. Eng.* **122**(5), 488–492 (2000).
11. L. Goubergrits et al., "Geometry of the human common carotid artery. A vessel cast study of 86 specimens," *Pathol. Res. Pract.* **198**(8), 543–551 (2002).
12. A. Daugherty, "Mouse models of atherosclerosis," *Am. J. Med. Sci.* **323**(1), 3–10 (2002).
13. J. Jawien, P. Nastalek, and R. Korbut, "Mouse models of experimental atherosclerosis," *J. Physiol. Pharmacol.* **55**(3), 503–517 (2004).
14. A. S. Plump et al., "Severe hypercholesterolemia and atherosclerosis in apolipoprotein E-deficient mice created by homologous recombination in ES cells," *Cell* **71**(2), 343–353 (1992).
15. J. A. Piedrahita et al., "Generation of mice carrying a mutant apolipoprotein E gene inactivated by gene targeting in embryonic stem cells," *Proc. Natl. Acad. Sci. U S A* **89**(10), 4471–4475 (1992).
16. S. Ishibashi et al., "Hypercholesterolemia in low density lipoprotein receptor knockout mice and its reversal by adenovirus-mediated gene delivery," *J. Clin. Invest.* **92**(2), 883–893 (1993).
17. Y. Nakashima et al., "ApoE-deficient mice develop lesions of all phases of atherosclerosis throughout the arterial tree," *Arterioscler. Thromb.* **14**(1), 133–140 (1994).
18. J. D. Smith and J. L. Breslow, "The emergence of mouse models of atherosclerosis and their relevance to clinical research," *J. Intern. Med.* **242**(2), 99–109 (1997).
19. J. L. Johnson and C. L. Jackson, "Atherosclerotic plaque rupture in the apolipoprotein E knockout mouse," *Atherosclerosis* **154**(2), 399–406 (2001).
20. C. Badea, L. W. Hedlund, and G. A. Johnson, "Micro-CT with respiratory and cardiac gating," *Med. Phys.* **31**(12), 3324–3329 (2004).
21. C. T. Badea et al., "4-D micro-CT of the mouse heart," *Mol. Imaging* **4**(2), 110–116 (2005).
22. L. W. Hedlund et al., "MR-compatible ventilator for small animals: computer-controlled ventilation for proton and noble gas imaging," *Magn. Reson. Imaging* **18**(6), 753–759 (2000).
23. F. Wiesmann et al., "High-resolution MRI with cardiac and respiratory gating allows for accurate in vivo atherosclerotic plaque visualization in the murine aortic arch," *Magn. Reson. Med.* **50**(1), 69–74 (2003).
24. J. Ruff et al., "Magnetic resonance imaging of coronary arteries and heart valves in a living mouse: techniques and preliminary results," *J. Magn. Reson.* **146**(2), 290–296 (2000).
25. T. Yamashita et al., "In vivo angiographic detection of vascular lesions in apolipoprotein E-knockout mice using a synchrotron radiation microangiography system," *Circ. J.* **66**(11), 1057–1059 (2002).
26. A. W. Wetzel et al., "Measurement and modeling of 4D live mouse heart volumes from CT time series," *Proc. SPIE* **6491**, 64910J (2007).
27. B. Fernandez et al., "The coronary arteries of the C57BL/6 mouse strains: implications for comparison with mutant models," *J. Anat.* **212**(1), 12–18 (2008).
28. D. Ahn et al., "Induction of myocardial infarcts of a predictable size and location by branch pattern probability-assisted coronary ligation in C57BL/6 mice," *Am. J. Physiol. Heart Circ. Physiol.* **286**(3), H1201–H1207 (2003).
29. X. Michalet et al., "Quantum dots for live cells, in vivo imaging, and diagnostics," *Science* **307**(5709), 538–544 (2005).
30. B. Ballou et al., "Noninvasive imaging of quantum dots in mice," *Bioconjug. Chem.* **15**(1), 79–86 (2004).
31. M. K. So et al., "Self-illuminating quantum dot conjugates for in vivo imaging," *Nat. Biotechnol.* **24**(3), 339–343 (2006).
32. N. Y. Morgan et al., "Real time in vivo non-invasive optical imaging using near-infrared fluorescent quantum dots," *Acad. Radiol.* **12**(3), 313–323 (2005).
33. D. R. Larson et al., "Water-soluble quantum dots for multiphoton fluorescence imaging in vivo," *Science* **300**(5624), 1434–1436 (2003).
34. M. E. Akerman et al., "Nanocrystal targeting in vivo," *Proc. Natl. Acad. Sci. U S A* **99**(20), 12,617–12,621 (2002).
35. Z. H. Ding, H. Zhu, and M. H. Friedman, "Coronary artery dynamics in vivo," *Ann. Biomed. Eng.* **30**(4), 419–429 (2002).
36. Z. H. Ding and M. H. Friedman, "Quantification of 3-D coronary arterial motion using clinical biplane cineangiograms," *Int. J. Card. Imaging* **16**(5), 331–346 (2000).
37. D. Kumar et al., "Distinct mouse coronary anatomy and myocardial infarction consequent to ligation," *Coron. Artery Dis.* **16**(1), 41–44 (2005).

38. Y. S. Chatzizisis et al., "Is left coronary system more susceptible to atherosclerosis than right? A pathophysiological insight," *Int. J. Cardiol.* **116**(1), 7–13 (2007).
39. I. Chung et al., "Description of the fluorescence intensity time trace of collections of CdSe nanocrystal quantum dots based on single quantum dot fluorescence blinking statistics," *Phys. Rev. E, Stat. Nonlin. Soft Matter Phys.* **73**(1), 011106 (2006).
40. S. F. Lee and M. A. Osborne, "Photodynamics of a single quantum dot: fluorescence activation, enhancement, intermittency, and decay," *J. Am. Chem. Soc.* **129**(29), 8936–8937 (2007).
41. M. Jonas et al., "Detecting single quantum dot motion with nanometer resolution for applications in cell biology," *IEEE Trans. Nanobiosci.* **5**(4), 246–250 (2006).
42. I. Texier and V. Josser, "In vivo imaging of quantum dots," *Methods Mol. Biol.* **544**, 393–406 (2009).
43. B. D. Hoit, N. Ball, and R. A. Walsh, "Invasive hemodynamics and force-frequency relationships in open- versus closed-chest mice," *Am. J. Physiol.* **273**(5 Pt 2), H2528–H2533 (1997).